Featured in Physics

Measurement of the prompt fission neutron spectrum from 800 keV to 10 MeV for ^{240}Pu(sf) and for the ^{240}Pu(n, f) reaction induced by neutrons of energy from 1–20 MeV

K. J. Kelly [1,*] M. Devlin [1] J. M. O'Donnell,[1] D. Neudecker,[1] C. Y. Wu [2] R. Henderson,[2] A. E. Lovell [1]
R. C. Haight,[1] E. A. Bennett [1] J. L. Ullmann,[1] N. Fotiades [1] and P. A. Copp[1]

[1]*Los Alamos National Laboratory, Los Alamos, New Mexico 87545, USA*
[2]*Lawrence Livermore National Laboratory, Livermore, California 94550, USA*

The presence of ^{240}Pu in nuclear fuels for reactors has resulted in high uncertainties in the results of reactor and nuclear transmutation calculations because of deficiencies in ^{240}Pu-related nuclear data. Specifically for the prompt fission neutron spectrum (PFNS) of ^{240}Pu, there is only one neutron-induced, (n, f), measurement at 0.85 MeV incident neutron energy and only one complete spontaneous fission, (sf), measurement. This limited availability of data does not sufficiently guide nuclear data evaluations of these quantities. Here, we report on a measurement of both the ^{240}Pu(sf) and the ^{240}Pu(n, f) PFNS, both over the emitted neutron energy range of 0.79–10.0 MeV, and from incident neutron energies of 1.0–20.0 MeV for the (n, f) reaction. Measurements were made with a hemispherical array of liquid scintillators at the high-energy Los Alamos Neutron Science Center white neutron source at the Weapons Neutron Research facility as part of the joint LANL-LLNL Chi-Nu experimental campaign to measure actinide fission neutron spectra. These measurements are the first of their kind, and provide clear experimental evidence for second-chance fission, third-chance fission, and pre-equilibrium neutron emission processes in neutron-induced fission of ^{240}Pu, and are the first ever measurements above 1 MeV incident neutron energy.

I. INTRODUCTION

As a common component of nuclear fuels, uncertainties in nuclear data associated with ^{240}Pu result in significant uncertainties for nuclear reactor and criticality safety calculations [1–4], and are similarly impactful for accelerator driven systems [5]. In terms of the nucleus itself, ^{240}Pu is unique in that it spontaneously fissions like ^{252}Cf, spontaneously emits α particles at a rate that is approximately a factor of 4 higher than that of ^{239}Pu, and displays a soft fission threshold at approximately 500 keV incident neutron energy similar to the $\approx$1.5 MeV threshold for fission of ^{238}U. Fission occurs below this threshold, but the cross section for fission below the threshold of approximately 500 keV is typically more than an order of magnitude smaller than for ^{239}Pu [6].

The features of ^{240}Pu described above have made measurements of the energy spectrum of neutrons emitted promptly from fission, i.e., the prompt fission neutron spectrum (PFNS), challenging. To date, there exist only two publications of the PFNS from ^{240}Pu(sf) spontaneous fission [7,8] and one for neutron-induced fission at an incident neutron energy $E_n^{\rm inc} = 0.85$ MeV [9]. Thus, there are no measurements of the ^{240}Pu(n, f) PFNS above $E_n^{\rm inc} = 0.85$ MeV [10]. However, the fission cross section and fission fragment anisotropy characteristics of the ^{240}Pu(n, f) reaction are fairly well known [11–13].

We describe here the first measurements of the ^{240}Pu(n, f) PFNS above $E_n^{\rm inc} = 0.85$ MeV, and the second ever measurement of this quantity. These measurements were carried out using the Chi-Nu experimental setup at Los Alamos National Laboratory with an altered data acquisition and analysis method compared to that applied to previous Chi-Nu measurements of the ^{235}U, ^{238}U, and ^{239}Pu neutron-induced PFNS [14–17]. As part of the process for obtaining a pure neutron-induced ^{240}Pu PFNS, the ^{240}Pu(sf) PFNS was also measured and is reported here. Given the detail with which the data acquisition, analysis, and covariance derivations were described in Refs. [14–17], the description of some aspects of this experiment that are repeated elsewhere are kept brief, primarily highlighting the differences between this work and the previous measurements. The experimental environment is described in Sec. II and data analysis procedures are described in Sec. III. The ^{240}Pu(sf) and ^{240}Pu(n, f) PFNS results are shown in Sec. IV. Final concluding remarks are given in Sec. V.

II. EXPERIMENTAL SETUP

The measurements described in this work were carried out at the Weapons Neutron Research (WNR) facility at the Los Alamos Neutron Science Center (LANSCE) [18]. A pulsed, 800 MeV proton beam generated a continuous spectrum of neutrons from near 800 MeV down to $\approx$10 s of keV via spallation reactions on a tungsten target. Neutrons traveling 15° to the left of the incident proton beam were collimated

---

and impinged on a parallel plate avalanche counter (PPAC) [19] target, fabricated at Lawrence Livermore National Laboratory, containing approximately 20 mg total of 99.875% pure ^{240}Pu located within the experimental flight path (WNR FP15L). The remaining contributions to the total target mass are 0.114% ^{242}Pu, with all other isotopes below 0.01%. The effect of contaminants was negligible in the data analysis. Note that this amount of material is approximately a factor of 5 lower than was used for previous Chi-Nu PFNS measurements of ^{235}U, ^{238}U, and ^{239}Pu. This reduced amount of material was used to reduce the PPAC count rates due to α particle detection to an acceptable level. Data for the PPAC and other signals described below were all acquired asynchronously utilizing a series of CAEN 1730B [20] digitizers.

The PPAC target displayed a 1-σ time resolution of less than 1 ns as indicated by the photofission peak from prompt γ rays from the neutron-production target. Incident neutrons from 1.0–20.0 MeV were measured via time of flight between a signal corresponding to the spallation reaction time, denoted t_0, and a fission detection in the PPAC at a time t_f. The incident neutron flight path was 21.5(1) m, yielding flight times from 1483.94–281.39 ns for $E_n^{\text{inc}} = 1.0$–20.0 MeV. Thus, the sub-nanosecond time resolution of the PPAC target was sufficient to allow uncertainties on the incident neutron beam energy to be ignored. Proton pulses were received with a 1.789 μs time spacing, resulting in a "wraparound" effect wherein neutrons below $E_n^{\text{inc}} \approx 0.7$ MeV arrive at the PPAC target simultaneously with higher-energy neutrons from the next proton pulse. The ^{240}Pu(n, f) fission threshold is $E_n^{\text{inc}} \approx 500$ keV, and neutrons of this energy arrive at the PPAC target simultaneously with neutrons of energy $E_n^{\text{inc}} = 20$ MeV from the next proton pulse. Therefore, the wraparound effect from lower-energy neutrons was safely ignored for this work. The proton pulses, generally termed "micropulses", are grouped into "macropulses" of 347 neighboring micropulses, and each macropulse is separated from neighboring macropulses by 8.3 ms.

Neutrons were detected with a 54-element EJ-309 [21] liquid scintillator detector array [14,15] spanning nine equally spaced θ angles from 30° to 150° relative to the incident neutron direction with six detectors per θ at ϕ polar angles of 0, 33, 66, 114, 147, and 180 ° relative to horizontal, all within the upper hemisphere. See Fig. 1 for a rendering of this array. Coincidences between neutron detections within this liquid scintillator array, detected at a time t_n, with PPAC detections at t_f were observed to display a 1-σ time resolution of 1.13(2) ns over the nominal 1.020(5) m flight path from PPAC center to the center of each liquid scintillator volume. Typical Chi-Nu PFNS measurements also utilize a Li-glass detector array [22–24] to measure low-energy neutrons from fission. However, the low efficiency of this array would have required experiment times on the order of a full LANSCE beam cycle, which was not feasible. Thus, only the liquid scintillator array was used for ^{240}Pu(n, f) measurements and instead each signal was split into two separate digitizer channels, one with a 2 V full scale typically employed for Chi-Nu measurements and the other with an 0.5 V full scale, such that the alternate configuration could yield improved sensitivity to lower emitted neutron energies and compensate for the lack of Li-glass
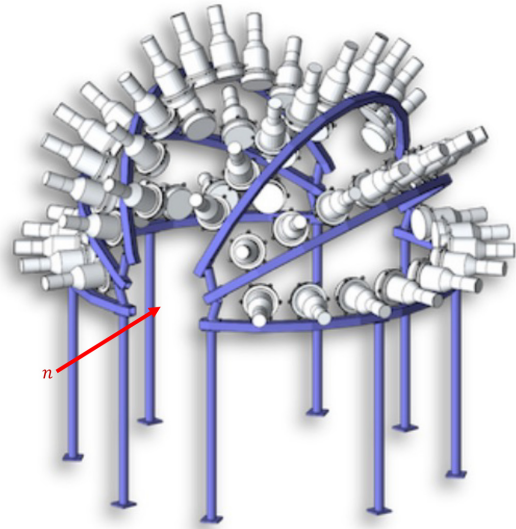

FIG. 1. A computer-generated rendering of the liquid scintillator detector system used for the results shown in this work. Incident neutrons enter from the lower-left side of the array, and the PPAC target was placed in the center of this array. This figure is a reproduction of Fig. 3 of Ref. [16].

measurement data. Throughout this paper, these two full scale signal ranges are termed "standard" and "alternate." In order to validate the extension of liquid scintillator data to lower energies, a measurement of the ^{240}Pu(sf) PFNS was attempted with the Li-glass detector system such that the ^{240}Pu(sf) PFNS could be confirmed prior to extracting the ^{240}Pu(n, f) PFNS. However, this also proved to be not feasible because of the low spontaneous fission rate of ^{240}Pu and, again, the low efficiency of this detector array. Therefore, the covariance for data at these lower energies, which are dominated by Monte Carlo N-particle (MCNP) simulation-based corrections and statistical uncertainties, required additional treatment to ensure that the uncertainties span the potential range of error of the results of this work as described in Sec. III.

III. DATA ANALYSIS

Analysis techniques applied to the ^{240}Pu(sf) and ^{240}Pu(n, f) data have some similarities, but also significant differences. Identical to all previous Chi-Nu PFNS measurements [14–17], corrections were applied to both the (n, f) and (sf) liquid scintillator and PPAC data to eliminate signal reflections within the cables, signal time walk, timing alignments of all detectors together, and to isolate neutron signals from γ rays using pulse-shape discrimination (PSD), and further purify the neutron signals using neutron kinematics relative to the fission detection times. These details are described thoroughly in Refs. [15–17,24], and are not elaborated upon here.

As opposed to previous Chi-Nu measurements where signals only within each macropulse were considered for further analysis, data outside of each macropulse and extended up to the beginning of each subsequent pulse were retained for
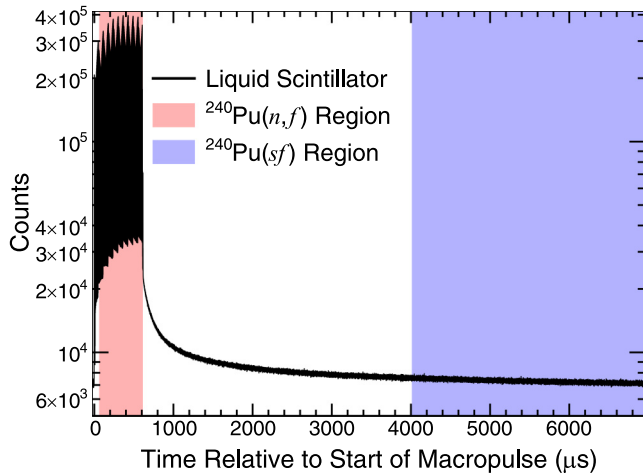
FIG. 2. The counts (black) before PSD, kinematics, coincidence, and other data analysis processes in a liquid scintillator over the course of a macropulse and the time leading up to the next macropulse. The time regions used for ^{240}Pu(n, f) and ^{240}Pu(sf) measurements are shaded in red (left) and blue (right), respectively.

analysis. Time coincidence ranges between fission and neutron events were considered within a t_n-t_f coincidence time window from -150 to $+350$ ns. Figure 2 shows counts obtained for a single liquid scintillator detector over the course of a macropulse and the time between one macropulse and the next. Time windows relative to the start of a macropulse chosen for (n, f) and (sf) data analysis are shown as red and blue shaded regions, respectively, in Fig. 2. The flux at WNR FP15L was filtered through a 0.5 in. thick borated polyethylene disk to reduce the already minimal contribution of sub-keV neutrons to the incident neutron flux. If sub-keV neutrons were present in the WNR FP15L incident neutron flux, the data collected from 4000 to 7000 μs relative to the start of the macropulse would correspond to approximately 0.15 to 0.05 eV of incident neutron energy, which is below the lowest resonance in the ^{240}Pu(n, f) cross section at approximately 1.0 eV [6]. However, the flux of neutrons with neutron energies this low is expected to be effectively nonexistent, and thus data analyzed from this time region are believed to be from the ^{240}Pu(sf) reaction. Incident neutron t_0 signals were not present in the (sf) data, and were excluded from the coincidence data analysis.

After obtaining the data spectra (i.e., the combined spectra of foreground and background counts) for both (n, f) and (sf) data, the (sf) contribution to (n, f) data was removed based on the counts observed above background and the relative time windows for measurement (see Sec. III C). The ^{240}Pu(sf) PFNS itself was also separately characterized using similar techniques for both (n, f) and (sf) data analysis after background subtraction. The different processes for background subtraction are described in Secs. III A and III B, respectively. The removal of the ^{240}Pu(sf) contribution to the ^{240}Pu(n, f) data is then discussed in Sec. III C, followed by the analysis to characterize the E_n^{inc}-dependent ^{240}Pu(n, f) and E_n^{inc}-independent ^{240}Pu(sf) PFNS in Sec. III D.

A. ^{240}Pu(n, f) background subtraction

As with many coincidence experiments, the dominant source of background was accidental, or random, coincidences. In other words, a coincidence was measured between the PPAC and a liquid scintillator that corresponded in reality to a background neutron in coincidence with a true fission event, a true fission neutron in coincidence with an uncorrelated fission, or another similar scenario. By far the dominant source of random coincidence signals was related to α particle detection signals in the PPAC. The intensity of this time- and beam-independent source of background accounted for $>90\%$ of the signals observed within a macropulse for the PPAC *after* a cut was placed on PPAC signals to initially remove α contamination from the data stream.

These and other contributions to the random-coincidence background in the (n, f) data analysis were accounted for with the method described in Ref. [25]. In short, the singles (i.e., pre-coincidence) data are used to define the Poisson probability of detecting neutrons at a specific time relative to a t_0 incident neutron signal for both neutron and fission detections. These data naturally have much higher statistical precision than the post-coincidence data. Based on these time distributions, the probability for detecting a neutron and a fission event within a chosen time coincidence window can be calculated directly (see Refs. [15,25,26]). This probability was then converted to background counts with a scaling factor corresponding to the number of t_0 signals in the data set. This random-coincidence background was defined separately for each t_0-t_f coincidence window corresponding to the bins of incident neutron energy reported in this work.

The random-coincidence background overwhelmed the foreground counts for these data to the point that even a 0.3% uncertainty on the random-coincidence background would result in a total uncertainty that is more than a factor of 3 higher than the sum of all remaining sources of uncertainty for these results. Thus, it was imperative that both the statistical and systematic uncertainty of the random-coincidence backgrounds be kept as low as possible. Luckily, as was described in Ref. [26], if a signal in a coincidence-detection experiment maintains a nearly constant rate (i.e., the PPAC with a beam- and time-independent high α-detection rate), the other detector (liquid scintillators in this case) can vary in any way without introducing an error in the random-coincidence background. In other words, the random-coincidence background method of Ref. [25] should work nearly perfectly for these data.

The accuracy of the random-coincidence background directly from this method was confirmed by shifting the t_f PPAC fission detection times as was done for previous Chi-Nu PFNS measurements in Refs. [15–17] in which no statistically significant difference was observed with or without including this additional component of the background typically added to account for systematic errors in the random-coincidence background. Thus, the random-coincidence backgrounds for the ^{240}Pu(n, f) data were obtained directly from the method itself, with a systematic uncertainty assigned according to Eq. (6) of Ref. [15]. A systematic uncertainty from run-to-run rate variations of 0.41% was calculated based on methods
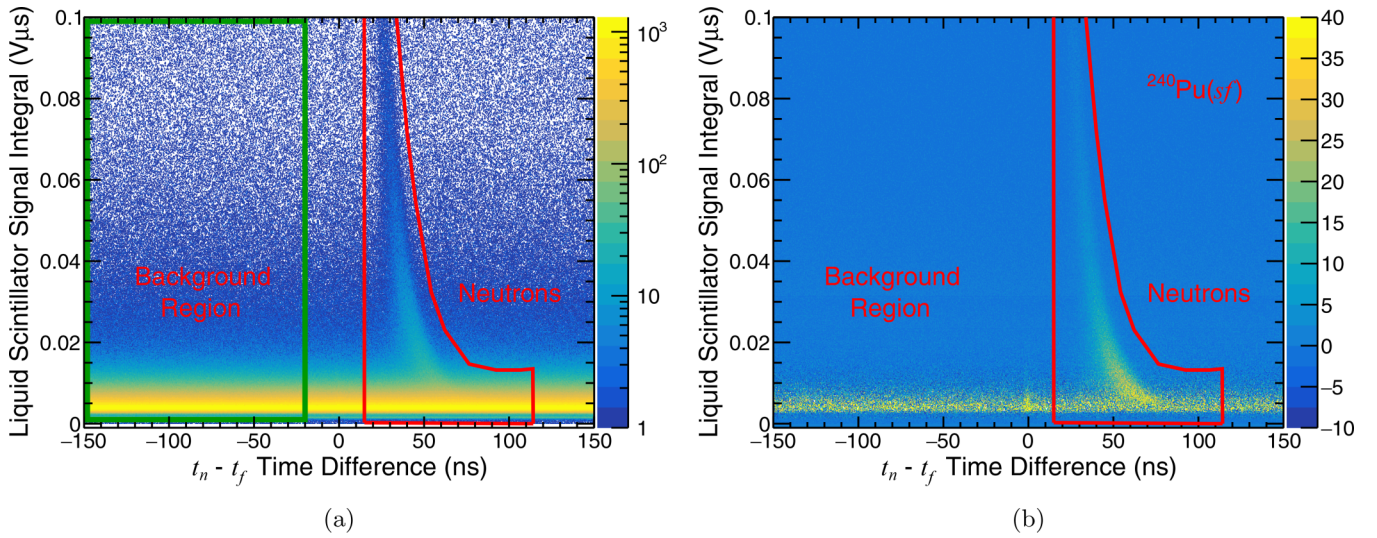
FIG. 3. Neutron kinematic data obtained for liquid scintillators corresponding to the ^{240}Pu(sf) region of Fig. 2. (a) shows these data before subtraction of random backgrounds obtained from the average of counts within the green boxed background region on the left of this panel, and (b) after subtraction. The neutron kinematic cut for fission neutrons is shown in red.

described in Refs. [15–17]. This uncertainty is approximately a factor of 3–4 smaller than for the ^{235}U data set [16], because of the more constant PPAC rate as described above, but the larger contribution of random-coincidence backgrounds to the total data set yielded a relative uncertainty nearly a factor of ≈ 7 higher than the ^{235}U result at high E_n^{out} where the impact of the background is the largest [$\approx 3\%$ for ^{235}U(n, f) near $E_n^{\text{out}} = 8$ MeV compared with $\approx 20\%$ or more for ^{240}Pu(n, f) in this work at the same E_n^{inc}].

B. ^{240}Pu(sf) background subtraction

Spontaneous fission data are fundamentally different from in-beam data because there are no t_0 signals from which to define a reference "start" time for a t_f or t_n detection window. While a pulsed, false trigger could be placed in the data stream, this was not done for the off-macropulse data utilized for the ^{240}Pu(sf) measurement described here. Instead, given that true fission-neutron coincidences can only occur at positive t_n-t_f coincidence time differences, the counts observed at negative times were used to define the random-coincidence background. This is illustrated in Fig. 3. Figure 3(a) shows ^{240}Pu(sf) data as the signal integral versus t_n-t_f data with a red line denoting the expected neutron kinematic cut for these data and a green shaded region showing the region studied for random-coincidence background assessments. For each row of signal integral and time bin within the background region, denoted d_{ik} with i and k indicating the x and y bin of the spectrum, the counts within the background region were averaged to obtain an average time-independent background as a function of time,

$$\bar{b}_k = \frac{1}{N_t} \sum_{i=0}^{N_t} d_{ik}, \tag{1}$$

where N_t is the number of time bins within the background region. The counts above background, denoted as the fore-

ground counts,

$$f_{ik} = d_{ik} - \bar{b}_k, \tag{2}$$

possess a correlation relating to the use of a constant $\bar{b}_k$ for each k signal integral row described by

$$\text{cov}[f_{ik}, f_{jl}] = \delta_{kl}[\delta_{ij}d_{ik} + \bar{b}_k], \tag{3}$$

where δ_{ij} and similar terms represent Kronecker δ functions. The spectrum of foreground counts following this procedure is shown in Fig. 3(b). The counts in the projected time spectrum, t_i, are described by

$$t_i = \sum_{k=1}^{N_k} c_{ik} f_{ik}, \tag{4}$$

where N_k is the total number of integral bins along the y axis and c_{ik} is a multiplicative factor that is unity if a bin is included within the neutron kinematic cut [red line in Fig. 3(a)] and is 0 otherwise, yielding a covariance of

$$\text{cov}[t_i, t_j] = \sum_{k=1}^{N_k} c_{ik} c_{jl}[\delta_{ij}d_{ik} + \bar{b}_k]. \tag{5}$$

The time spectrum following the time-constant background removal process above was then transformed to energy space by converting each time bin limit to energy space via

$$E = m_n c^2 \left[\left(1 - \left(\frac{l}{t_n c} \right)^2 \right)^{-\frac{1}{2}} - 1 \right], \tag{6}$$

where m_n is the neutron mass, c is the speed of light, and l is the flight path appropriate for each PPAC-liquid scintillator combination. The typical energy binning for Chi-Nu PFNS measurements is a logarithmic 20 bins per decade, and it is desirable to maintain this same binning scheme for direct comparisons to other Chi-Nu results as was done in

Refs. [16,17,27]. Time bins are reorganized into counts in energy bin p defined as, E_p, as

$$E_p = \sum_{i=1}^{N_t} \phi_{ip} t_i, \tag{7}$$

where ϕ_{ip} is the fractional overlap of time bin t_i with energy bin E_p, yielding a covariance

$$\mathrm{cov}[E_p, E_q] = \sum_{i=1}^{N_t} \sum_{j=1}^{N_t} \phi_{ip} \phi_{jq} \mathrm{cov}[t_i, t_j]. \tag{8}$$

The use of negative-time coincidence detections in this way induces a correlation between E_p values originating from the use of a constant average background, $\bar{b}_k$, hence the above calculation. This covariance is important for understanding the covariance of the ^{240}Pu(sf) PFNS discussed in Sec. III D.

C. ^{240}Pu(sf) removal from ^{240}Pu(n, f) data

Having defined the counts above background, i.e., foreground, for both ^{240}Pu(sf) and ^{240}Pu(n, f), the (sf) component was removed from in-beam data for each incident neutron energy, E_α where Greek indices represent incident neutron energies, according to a ratio, r_α, defined to be

$$r_\alpha = N_\mu \frac{I_s T_\alpha}{I_\alpha T_s}. \tag{9}$$

Here, T_s and T_α are the time windows for spontaneous fission (see Fig. 2) and E_α, respectively, N_μ is the number of micropulses in a macropulse (i.e., a multiplicative factor for the time window T_α), and I_s and I_α are the integrals of foreground counts for (sf) and E_α, respectively. The E_n^{inc}-correlated covariance for these ratios is written as

$$\mathrm{cov}[r_\alpha, r_\beta] = r_\alpha r_\beta \left\{ \frac{\mathrm{cov}[I_\alpha, I_\beta]}{I_\alpha I_\beta} + \frac{\mathrm{var}[I_s]}{I_s^2} \right\}. \tag{10}$$

Correlations between incident neutron energies, α and β, have been part of the focus for previous Chi-Nu PFNS measurements [15,16], but these correlations are generally introduced from the correlated MCNP-based analysis paths followed *after* the data are processed to the point of a final (n, f) foreground spectrum. Therefore, we treat $\mathrm{cov}[I_\alpha, I_\beta]$ as diagonal at this point of the analysis, yielding

$$\mathrm{cov}[r_\alpha, r_\beta] = r_\alpha r_\beta \left\{ \frac{\delta_{\alpha\beta} \mathrm{var}[I_\alpha]}{I_\alpha^2} + \frac{\mathrm{var}[I_s]}{I_s^2} \right\}. \tag{11}$$

For reference, with N_μ nominally equal to 347 micropulses per macropulse, the values of r_α as a function of E_α are shown in Table I, with uncertainties propagated from I_α and I_s values. The largest contamination fraction corresponds to lowest E_α energy range of $E_\alpha = 1.0$–2.0 MeV since it corresponds to the largest time integration window, but even then the ^{240}Pu(sf) is only expected to contribute 1.373(3)% of the observed spectrum. This contamination is reduced to 0.258(1)% at $E_\alpha = 19.0$–20.0 MeV.

The foreground counts for the ^{240}Pu(n, f) data, $f_{\alpha,p}$, after subtraction of both random-coincidence backgrounds according to the method described in Sec. III A and the ^{240}Pu(sf), can

TABLE I. Percentage contamination of ^{240}Pu(sf) within the ^{240}Pu(n, f) data corresponding to each listed incident neutron energy range.

E_n^{inc} (MeV)	Contamination (%)
1.0–2.0	1.373(3)
2.0–3.0	0.794(2)
3.0–4.0	0.655(1)
4.0–5.0	0.563(1)
5.0–5.5	0.519(1)
5.5–6.0	0.504(1)
6.0–7.0	0.422(1)
7.0–8.0	0.364(1)
8.0–9.0	0.342(1)
9.0–10.0	0.338(1)
10.0–11.0	0.348(1)
11.0–12.0	0.356(1)
12.0–13.0	0.354(1)
13.0–14.0	0.348(1)
14.0–15.0	0.326(1)
15.0–16.0	0.310(1)
16.0–17.0	0.291(1)
17.0–18.0	0.283(1)
18.0–19.0	0.270(1)
19.0–20.0	0.258(1)

be written as

$$f_{\alpha p} = d_{\alpha p} - b_{\alpha p} - r_\alpha E_p \tag{12}$$

with

$$\mathrm{cov}[f_{\alpha p}, f_{\beta q}] = r_\alpha r_\beta \mathrm{cov}[E_p, E_q] + E_p E_q \mathrm{cov}[r_\alpha, r_\beta] \\ + \delta_{\alpha\beta} \delta_{pq} (d_{\alpha p} + b_{\alpha p}). \tag{13}$$

Thus, for this analysis in which counts from the same ^{240}Pu(sf) PFNS is removed from each ^{240}Pu(n, f) spectrum (though at different contamination amounts), a correlation is induced across incident and outgoing neutron energies prior to other corrections.

D. ^{240}Pu(sf) and ^{240}Pu(n, f) characterization and PFNS extraction

Data analysis procedures for both ^{240}Pu(sf) and ^{240}Pu(n, f) to account for neutron detection efficiency, neutron environmental response, and other experimental effects required for converting foreground counts to a PFNS were identical to each other, and near identical to the process followed for previous Chi-Nu PFNS measurements [15–17]. Rather than define a one-dimensional function of neutron-detection efficiency from a measurement of the ^{252}Cf(sf) PFNS or equivalently measuring directly relative to ^{252}Cf(sf), PFNS results were extracted utilizing a two-dimensional neutron response matrix technique [28,29] developed using highly-detailed and validated MCNP simulations of the experimental environment [15,22,23,28,29]. This matrix allowed for the distortion of a series of template PFNS distributions spanning ^{252}Cf, ^{235}U, ^{238}U, and ^{239}Pu from the input distribution to the measured spectrum to be calculated [24,30]. In opposition to

assumptions implicitly made when considering measurements using only a ^{252}Cf(sf) reference spectrum or ^{252}Cf-based efficiency, the distortions observed for different spectra are significantly different. A primary benefit of the analysis carried out in this work over ^{252}Cf-based analyses is that the differences in the spectrum distortion, which reflects environmental neutron interactions, neutron detection efficiency, the physics of the detection mechanisms, and more, can be incorporated as a covariance assigned to the potential errors of the method itself. This is not possible when measuring relative to ^{252}Cf(sf), where the assumption is typically that ^{252}Cf is close enough to the desired neutron-induced PFNS that the ^{252}Cf(sf) PFNS spectrum distortion is negligibly different.

A primary concern for matching MCNP simulations to data is the definition of parameters, such as resolution for timing and pulse integral and the conversion of energy deposited in a detector volume to the light observed in a detector. The potential for error from these parameters are also typically most important at the high- and low-energy edges of the spectrum, where detector thresholds become important. These parameters in past Chi-Nu experiments have been defined well based on observations of the features in Li-glass data relating to the ^{6}Li(n, t) reaction, which validated MCNP parameters for liquid scintillator data in the overlap region between these detectors. However, the low efficiency of the Chi-Nu Li-glass detector array did not allow for a measurement of the ^{240}Pu(n, f) PFNS. Instead, an attempt was made to measure the ^{240}Pu(sf) PFNS with the Chi-Nu Li-glass detector system, which would then validate the low-energy extension of liquid scintillator data for both (sf) and (n, f) data. Unfortunately, this also did not yield useful results, and thus the covariance associated with the MCNP parameters impacting the low-energy edge of the liquid scintillator PFNS measurement was increased by a factor of 4 to account for any additional systematic uncertainties.

As with previous Chi-Nu PFNS measurements, MCNP-based corrections for fission fragment anisotropy and PPAC fission fragment detection efficiency were applied. The anisotropy of fragments emitted from neutron-induced fission of ^{240}Pu was measured by [11–13] to fairly high precision and was observed of similar magnitude to ^{235}U(n, f). This anisotropy was incorporated into observations of the relationship of emitted neutron angles and energies from fission as a function of fragment emission angle, generated with CGMF calculations [31], to measured neutron angles and energies via time of flight also as a function of fragment emission angle, generated via MCNP simulations of the emitted neutron energies and angles for each fragment. These calculations allowed for calculations of the impact on the PFNS at each incident and outgoing neutron energy from differences in fragment emission angles.

Additionally, as with all planar fission detectors, the PPAC efficiency for detecting a fission event changes as a function of the fission fragment emission angle which can be most easily observed as a change in the average neutron energy from fission as a function of angle relative to the target surface. A bias function representing this angular PPAC efficiency curve was applied to this transfer function between fragment emission angle and observed neutron energy via time

of flight. The potential for bias on the measured PFNS from fragment anisotropy and angular PPAC efficiency was studied with these MCNP simulations, with CGMF-generated fragment emission anisotropies and angles modified according to the fragment detection efficiency, and was used to generate a combined covariance for these possible effects. This process is identical to that carried out for previous Chi-Nu measurements [15–17], and the reader is referred specifically to Ref. [15] for details on this process. As was observed for previous measurements, these effects were generally small owing to the integration over a symmetric and wide range of neutron emission angles, and were especially small when compared to the now dominant sources of uncertainty from other backgrounds present in these data as well as the increased uncertainty from MCNP parameter definition.

E. Combination of split liquid scintillator signals and the covariance of the final results

The task of generating a single PFNS from 0.79 to 10 MeV amounted to a process of combining data from the two alternate liquid scintillator DAQ settings. This process was nearly identical to that followed for combining Li-glass and liquid scintillator data from previous measurements [15–17,32] (see specifically Sec. V of Ref. [15]), where here the "alternate" gain data were incorporated into the covariance analysis in a nearly identical way as the Li-glass data were in Refs. [15–17]. Therefore, we do not repeat the covariance calculations for this method here, though we note some important differences in the covariance calculations below.

Unlike previous Chi-Nu measurements with completely separate experiments for Li-glass and liquid scintillator detector measurements, here the standard and alternate gain results were extracted from the same light deposition into the scintillator liquid itself. Therefore, there is a strong correlation expected between the *statistical* precision of these results in the overlap region between them. This correlation factor is difficult to track precisely, but is very likely >0.9 with 1.0 representing a purely positive correlation. The statistical uncertainties in the overlap region between these detectors were treated as purely positively correlated (correlation coefficient $= 1$) in order to obtain an upper limit of the total uncertainty resulting from this correlation.

Finally, for removal of the (sf) component of the PFNS from the (n, f) results, systematic uncertainties from the MCNP-based data neutron scattering corrections were excluded because these methods were identically applied to both results and are therefore fully correlated. These uncertainties naturally drop out of the covariance analysis due to this correlation. Thus, the statistical precision of the (sf) result is the dominant contributor to the total uncertainty resulting from removing the (sf) contamination from the (n, f) results. An example of the partial relative uncertainties for the ^{240}Pu(n, f) results at $E_n^{\text{inc}} = 2.0-3.0$ MeV is shown in Fig. 4.

IV. RESULTS

In the following we first discuss the ^{240}Pu(sf) results in Sec. IV A, compared with the only other measurements of this quantity by Alexandrova *et al.* [7] in 1974 and the much
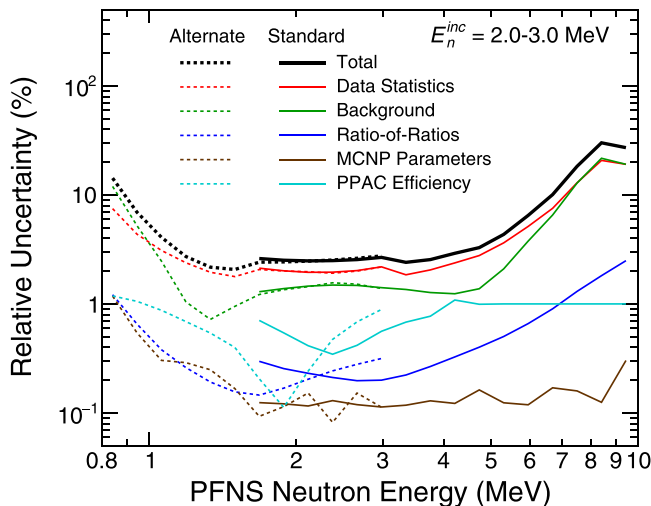
FIG. 4. Relative uncertainty trend for the $E_n^{inc} = 2.0$–3.0 MeV ^{240}Pu(n, f) PFNS. Note that the "Data Statistics" uncertainties were assumed to be fully correlated in the overlap region between the standard and alternate gain data.

more recent measurement by Gerasimenko *et al.* [8] in 2002. Results for the ^{240}Pu(n, f) PFNS were then divided according to the neutron-induced fission reaction channels available at different incident neutron energies.

Results from fission that proceeds only through neutron capture followed by nuclear fission of a ^{241}Pu nucleus, referred to as first-chance fission, are discussed in Sec. IV B for $E_n^{inc} = 1.0$ to 5.0 MeV. Those from fission that may proceed either through first-chance fission or via fission of a ^{240}Pu nucleus following the evaporation of a pre-fission neutron (second-chance fission) are shown in Sec. IV C for $E_n^{inc} = 5.0$
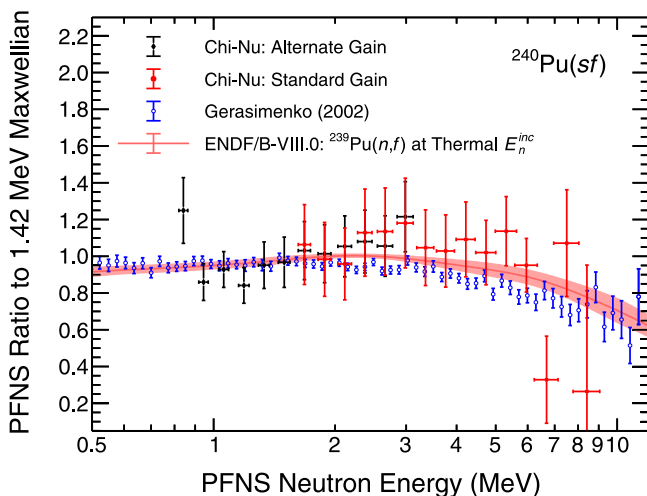

FIG. 5. The present results for standard (black diamonds) and alternate gain (red circles) liquid scintillator data are shown for the ^{240}Pu(sf) PFNS compared with the results from Gerasimenko *et al.* [8] (blue open circles). The red line and shaded region corresponds to the ENDF/B-VIII.0 evaluation of the ^{239}Pu(n, f) PFNS at thermal E_n^{inc}, as opposed to ^{240}Pu(sf). The data are shown as a ratio to a 1.42 MeV Maxwellian distribution.

to 10.0 MeV. Lastly, Sec. IV D shows results for $E_n^{inc} = 10$ to 20 MeV that may proceed via first- or second-chance fission, or via two additional processes that typically become available at approximately the same energy: third-chance fission, in which two pre-fission neutrons are emitted before a ^{239}Pu nucleus fissions, and by the pre-equilibrium neutron emission process in which a neutron scattering reaction precedes fission of a ^{240}Pu nucleus. These possible paths for fission are discussed in more detail in Ref. [14]. Note that there are no other measurements to compare with for results for any incident neutron energy range shown in this work. Finally, as an alternate method of viewing these results, the integrated mean PFNS energies, $\langle E \rangle$, are discussed in Sec. IV E.

A. ^{240}Pu(sf)

The results for the spontaneous fission PFNS of ^{240}Pu are shown in Fig. 5. Nuclear data evaluations of this spectrum are not reliable at the present time. We instead compare with the ENDF/B-VIII.0 evaluation of the ^{239}Pu(n, f) spectrum at thermal E_n^{inc} because this reaction also results in a ^{240}Pu nucleus undergoing fission. However, it should be noted that the interpretations of this comparison are limited by the fact that the excitation energy of the ^{240}Pu nucleus prior to fission is different for ^{240}Pu(sf) and thermal E_n^{inc} ^{239}Pu(n, f), and this can create differences in the PFNS from these two reactions. The literature results from Gerasimenko *et al.* [8] are shown for comparison as well. These data were reported as a ratio to ^{252}Cf(sf), defined to be a 1.42 MeV Maxwellian in the process of extracting a Maxwellian temperature for their data, but were also corrected for random-coincidence backgrounds, environmental neutron scattering from surrounding materials, and other important corrections. Thus, with the exception of the technique of measuring relative to ^{252}Cf(sf), these data appear to be carefully analyzed and trustworthy.

The only other measurement of the ^{240}Pu(sf) by Alexandrova *et al.* [7] who reported their data with no uncertainty information, focusing primarily on the determination of a Maxwellian temperature of 1.26 MeV for their analysis. This temperature is markedly lower than the 1.371(4) MeV determined by Gerasimenko *et al.* [8]. Therefore, in the absence of reliable data and uncertainties, we do not show these data for comparison. Unfortunately, there do not appear to be any reasonable nuclear data evaluations of the ^{240}Pu(sf) either, and thus we only compare with Gerasimenko *et al.* data.

While the granularity and uncertainties of the present results are not to the level of the Gerasimenko *et al.* data, the present results agree well within uncertainties with Gerasimenko *et al.* The agreement of the present results with the literature data of Gerasimenko *et al.* [8] validates the results for the ^{240}Pu(n, f) PFNS shown in the subsequent sections. Corrections of the in-beam PFNS for the ^{240}Pu(sf) contribution are effectively negligible.

B. ^{240}Pu(n, f) - 1.0–5.0 MeV

In this energy range, where the only neutron-induced fission reaction available is first-chance fission of ^{241}Pu, the PFNS is only expected to slightly increase at higher outgoing neutron energies based on present nuclear data evaluations
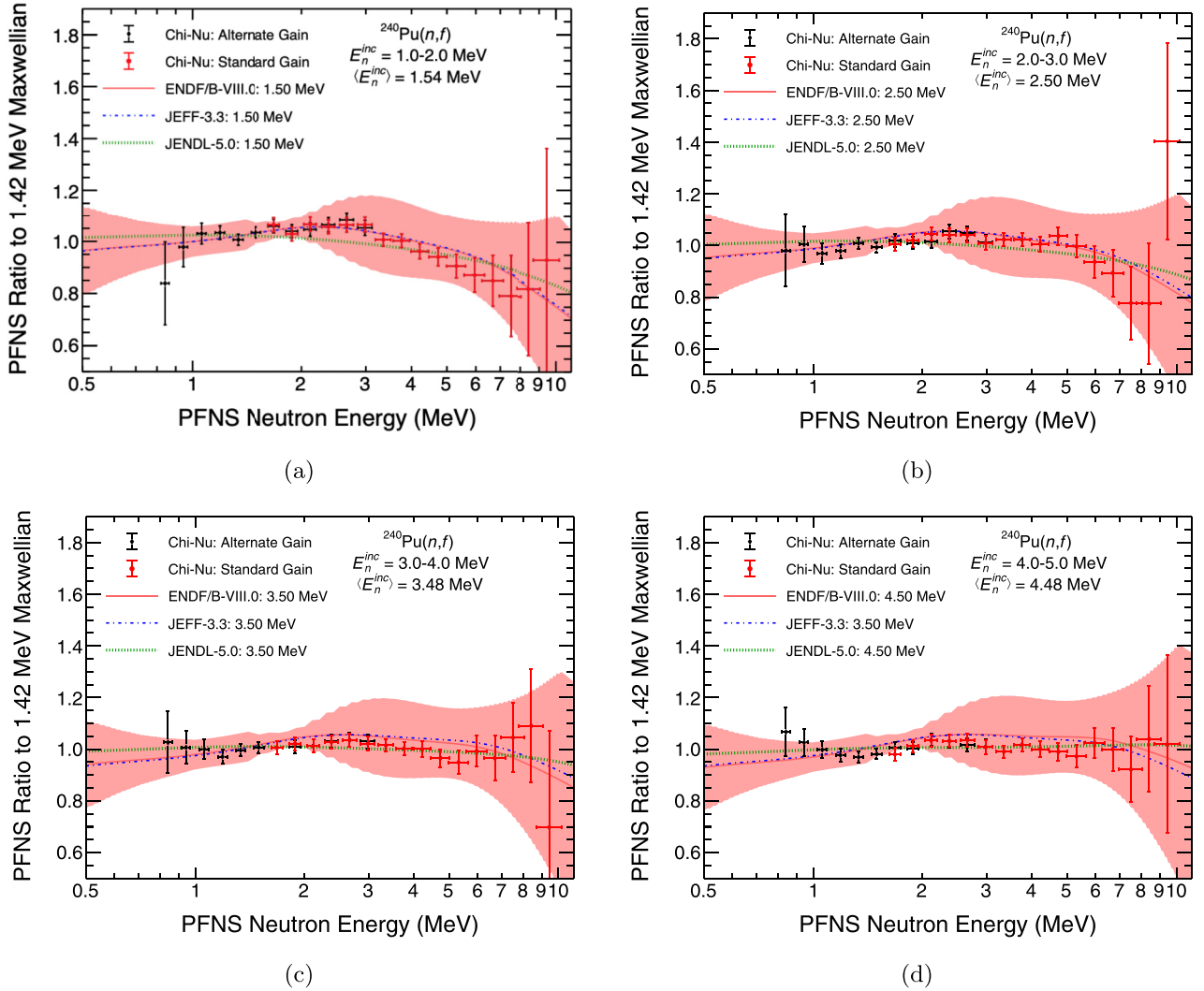
FIG. 6. The present results for standard (black diamonds) and alternate gain (red circles) liquid scintillator data are shown for (a) $E_n^{inc} =$ 1.0–2.0, (b) 2.0–3.0, (c) 3.0–4.0, and (d) 4.0–5.0 MeV, corresponding to average incident neutron energy, $\langle E_n^{inc} \rangle$, values of 1.54, 2.50, 3.48, and 4.48 MeV, respectively. ENDF/B-VIII.0 [6] evaluations are shown as solid red lines, JEFF-3.3 [33] as the dash-dotted blue lines, and JENDL-5.0 [34] as dotted green lines. The red shaded region corresponds to the uncertainty of the ENDF/B-VIII.0 evaluation on each plot. All other evaluation uncertainties can be assumed to be similar. All data are shown as a ratio to a 1.42 MeV Maxwellian distribution.

and as observed from measurements of ^{235}U, ^{238}U, and ^{239}Pu. Indeed, as seen in Figs. 6(a)–6(d), the PFNS closely resembles a Maxwellian distribution of 1.42 MeV below $E_n^{out} \approx 5$ MeV with a high-energy tail that increases with increasing incident energy. The present results agree within uncertainties with all evaluations shown, and there is little variation between the various evaluations. As with the ^{240}Pu(n, f) PFNS in these and all other E_n^{inc} ranges shown in this work, there are no literature data to compare with, and so all ^{240}Pu(n, f) results in this work are the first of their kind.

C. ^{240}Pu(n, f) - 5.0–10.0 MeV

The possibility for the second-chance fission process begins above $E_n^{inc} = 5.0$ MeV. The pre-fission neutron evaporated in this process can not be distinguished experimentally from the post-fission neutrons typically thought of as PFNS

neutrons, and so they are reported together here as well as in nuclear data evaluations. Beginning in Fig. 7(c) corresponding to $E_n^{inc} = 6.0$–7.0 MeV and even slightly in Fig. 7(a) ($E_n^{inc} =$ 5.5–6.0 MeV), the JENDL-5.0 evaluation starts to show a low-energy excess in the PFNS characteristic of the second-chance fission process. While there may be a hint of this feature from $E_n^{inc} = 6.0$–7.0 MeV in the present data, it is clearly present in Fig. 7(d) showing results for $E_n^{inc} = 7.0$–8.0 MeV, though it does not appear to produce as large of a distortion on the spectrum as predicted by JENDL-5.0. This feature becomes more subtle at higher E_n^{inc} values, as it increases in E_n^{out} with increasing E_n^{inc}.

Notably, while the ENDF/B-VIII.0 and JEFF-3.3 libraries do include multichance (i.e., second- and third-chance) fission treatments, the presence of this feature is much less pronounced. While the present results agree well within uncertainties with all evaluations in the $E_n^{inc} = 5.0$–10.0 MeV
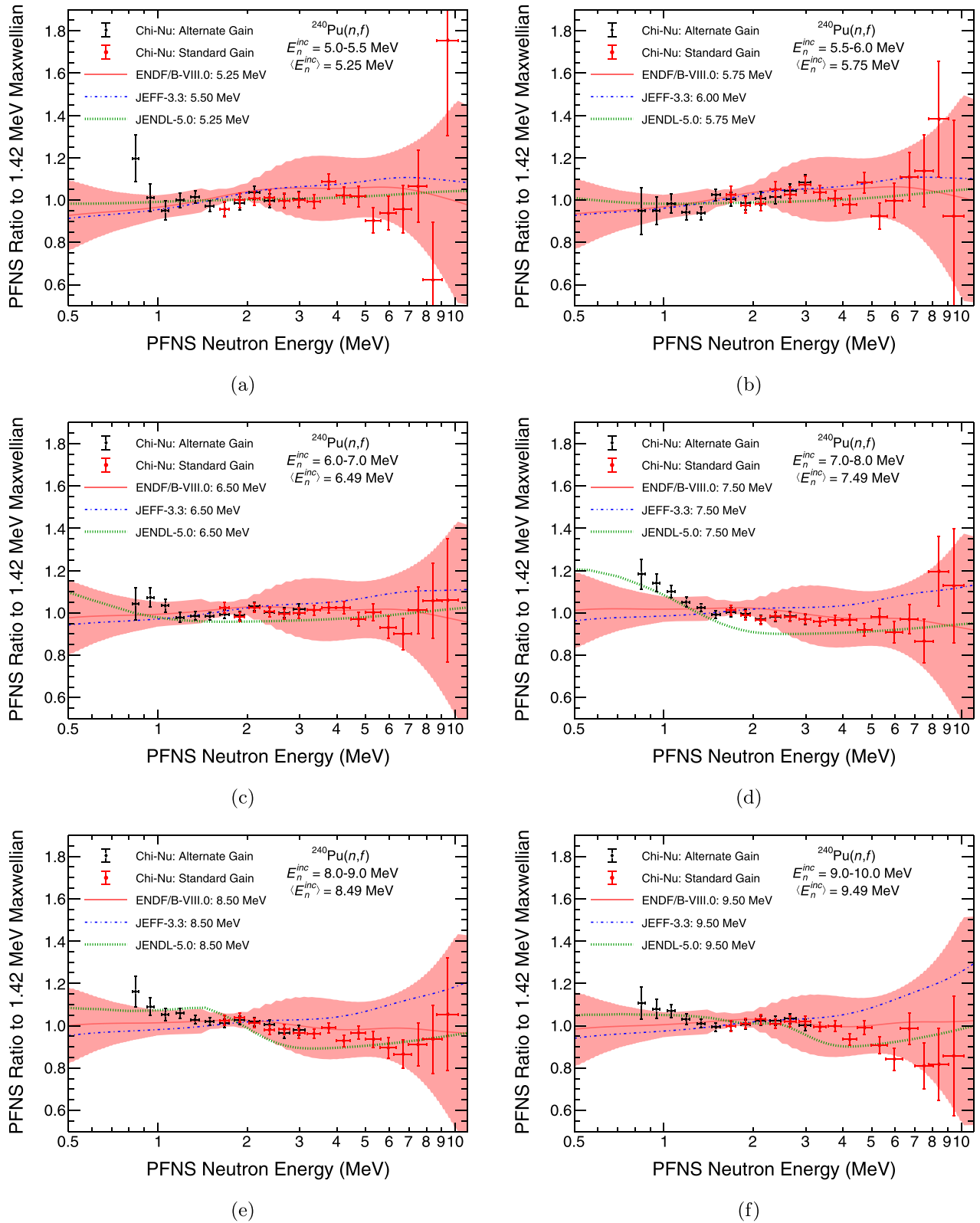
FIG. 7. The present results for standard (black diamonds) and alternate gain (red circles) liquid scintillator data are shown for (a) $E_n^{\text{inc}} = 5.0$–5.5, (b) 5.5–6.0, (c) 6.0–7.0, (d) 7.0–8.0 MeV, (e) 8.0–9.0, and (f) 9.0–10.0 MeV, corresponding to average incident neutron energy, $\langle E_n^{\text{inc}} \rangle$, values of 5.25, 5.75, 6.49, 7.49, 8.49, and 9.49 MeV, respectively. ENDF/B-VIII.0 [6] evaluations are shown as solid red lines, JEFF-3.3 [33] as the dash-dotted blue lines, and JENDL-5.0 [34] as dotted green lines. The red shaded region corresponds to the uncertainty of the ENDF/B-VIII.0 evaluation on each plot. All other evaluation uncertainties can be assumed to be similar. All data are shown as a ratio to a 1.42 MeV Maxwellian distribution.
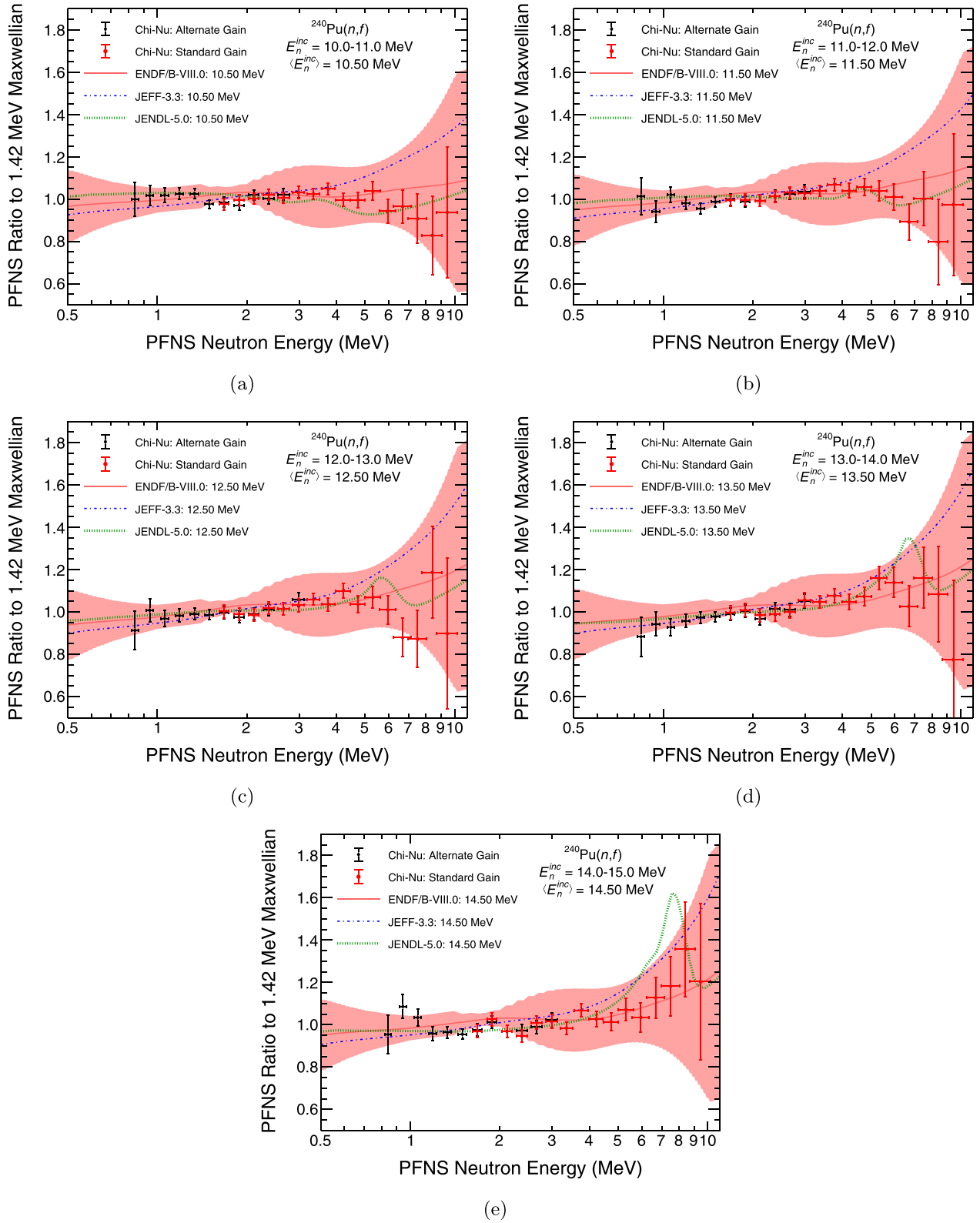
(a)

(b)

(c)

(d)

(e)

FIG. 8. The present results for standard (black diamonds) and alternate gain (red circles) liquid scintillator data are shown for (a) $E_n^{\mathrm{inc}} =$ 10.0–11.0, (b) 11.0–12.0, (c) 12.0–13.0, (d) 13.0–14.0, and (e) 14.0–15.0 MeV, corresponding to average incident neutron energy, $\langle E_n^{\mathrm{inc}} \rangle$, values of 10.50, 11.49, 12.51, 13.51, and 14.51 MeV, respectively. ENDF/B-VIII.0 [6] evaluations are shown as solid red lines, JEFF-3.3 [33] as the dash-dotted blue lines, and JENDL-5.0 [34] as dotted green lines. The red shaded region corresponds to the uncertainty of the ENDF/B-VIII.0 evaluation on each plot. All other evaluation uncertainties can be assumed to be similar. All data are shown as a ratio to a 1.42 MeV Maxwellian distribution.
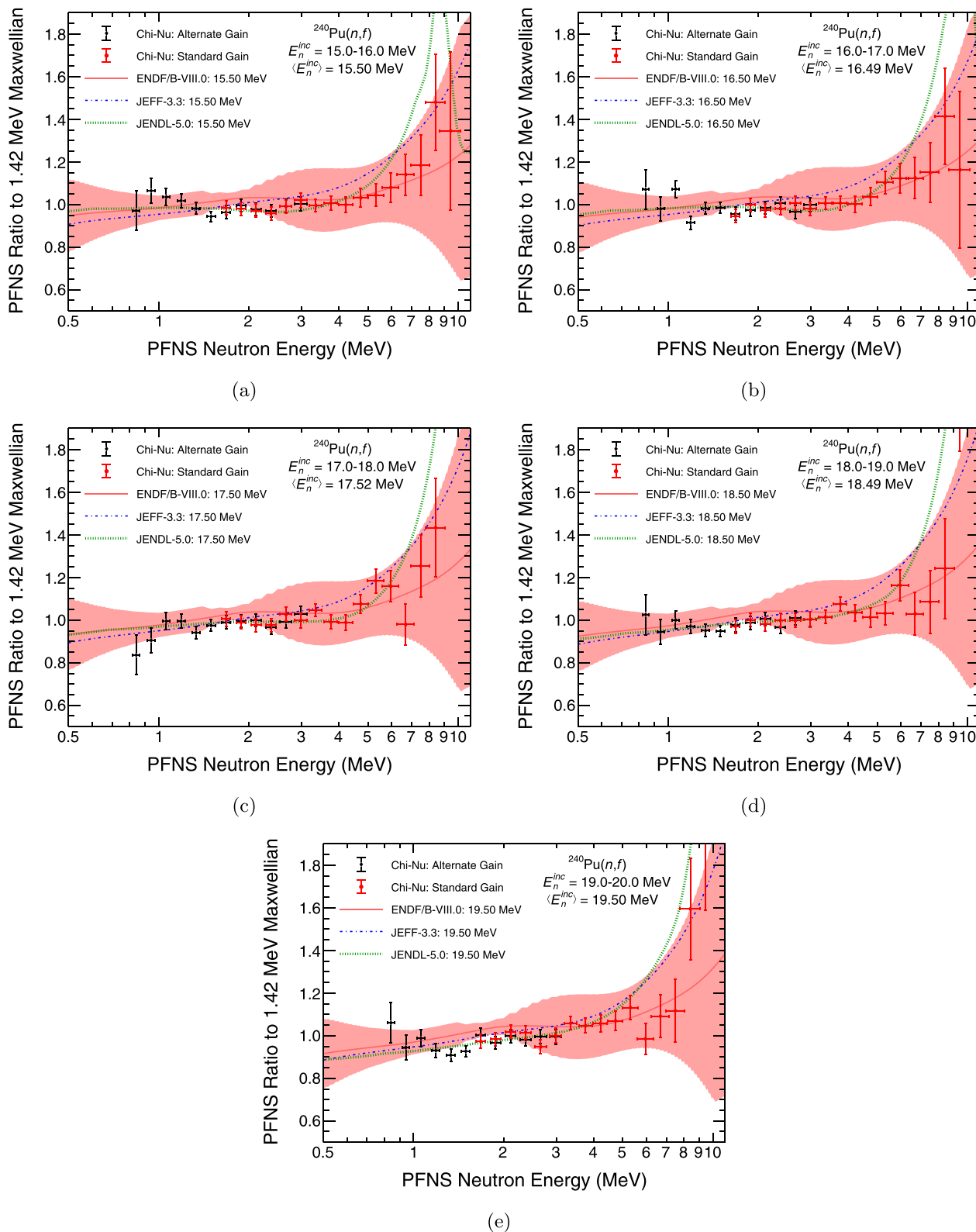
(a)

(b)

(c)

(d)

(e)

FIG. 9. The present results for standard (black diamonds) and alternate gain (red circles) liquid scintillator data are shown for (a) $E_n^{inc} =$ 15.0–16.0, (b) 16.0–17.0, (c) 17.0–18.0, (d) 18.0–19.0, and (e) 19.0–20.0 MeV, corresponding to average incident neutron energy, $\langle E_n^{inc} \rangle$, values of 15.51, 16.49, 17.52, 18.49, and 19.51 MeV, respectively. ENDF/B-VIII.0 [6] evaluations are shown as solid red lines, JEFF-3.3 [33] as the dash-dotted blue lines, and JENDL-5.0 [34] as dotted green lines. The red shaded region corresponds to the uncertainty of the ENDF/B-VIII.0 evaluation on each plot. All other evaluation uncertainties can be assumed to be similar. All data are shown as a ratio to a 1.42 MeV Maxwellian distribution.

range, the data appear to suggest a magnitude of second-chance fission in between those of JEFF-3.3 and JENDL-5.0. Lastly, as will be reiterated in Sec. IV E, the JEFF-3.3 evaluation appears to trend significantly higher than the data and the other evaluations, especially for $E_n^{\mathrm{inc}} = 8.0$–10.0 MeV in Figs. 7(e) and 7(f).

D. ^{240}Pu(n, f) - 10.0–20.0 MeV

Both third-chance fission of a ^{239}Pu nucleus and pre-equilibrium neutron emission preceding fission of ^{240}Pu become possible above $E_n^{\mathrm{inc}} = 10$ MeV with typical thresholds for these processes near $E_n^{\mathrm{inc}} = 11.0$–12.0 MeV. While third-chance fission manifests as a low-E_n^{out} excess in the PNFS similar to the effect of second-chance fission, pre-equilibrium neutron emission produces instead a peak in the spectrum, relative to a Maxwellian, at higher E_n^{out}. It is difficult to determine any clear third-chance fission features in the ^{240}Pu(n, f) reaction from the PFNS itself, though there is a small signature of this process seen in the $\langle E \rangle$ trends in Sec. IV E from $E_n^{\mathrm{inc}} = 13.0$–15.0 MeV. Similarly, none of the evaluations predict a very strong third-chance fission component, in agreement with the data.

The pre-equilibrium neutron emission feature can be seen in both the data and in the JENDL-5.0 evaluation as a peak from $E_n^{\mathrm{out}} = 4.0$–6.0 MeV in Fig. 8(b), corresponding to $E_n^{\mathrm{inc}} = 11.0$–12.0 MeV, and moving up to higher E_n^{out} with increasing E_n^{inc}. This peak is difficult to observe in the data above $E_n^{\mathrm{inc}} = 15.0$ MeV, but can be seen from Figs. 8(b)– 8(d). Based specifically on Figs. 8(c) and 8(d), it appears that the pre-equilibrium peak in JENDL-5.0 is slightly higher in E_n^{out} than in the present data, suggesting that thresholds relating to this process are slightly too low. This feature proceeds towards higher energies in Figs. 9(a)–9(e), though the statistical precision of the data make it difficult to see in the spectra themselves.

We note here the clear lack of pre-equilibrium features in the JEFF-3.3 and ENDF/B-VIII.0 libraries. Regarding the ENDF/B-VIII.0 PFNS evaluation, this evaluation was adopted from ENDF/B-VII.1 [35], which is stated to be based on data for the average neutron multiplicity from fission, $\bar{\nu}$, given the lack of any experimental data on the ^{240}Pu(n, f) PFNS. Multichance fission probabilities are quoted in Ref. [35], but no mention of pre-equilibrium processes is given, and it appears to not be present in the evaluation at all. The JEFF-3.3 ^{240}Pu(n, f) PFNS evaluation is similarly translated directly from the JEFF-3.2 library [36], and appears to also lack the presence of pre-equilibrium neutron emission processes.

E. Mean PFNS energy

The mean PFNS energies, $\langle E \rangle$, were calculated as an E_n^{out}-weighted average of the PFNS over the E_n^{out} range reported in this work for both the data and the ENDF/B-VIII.0, JEFF-3.3, and JENDL-5.0 libraries. The results of these calculations are shown in Fig. 10. Below the threshold for second-chance fission of approximately $E_n^{\mathrm{inc}} = 5.5$–6.0 MeV, all evaluations agree generally well with the data and with each other. How-
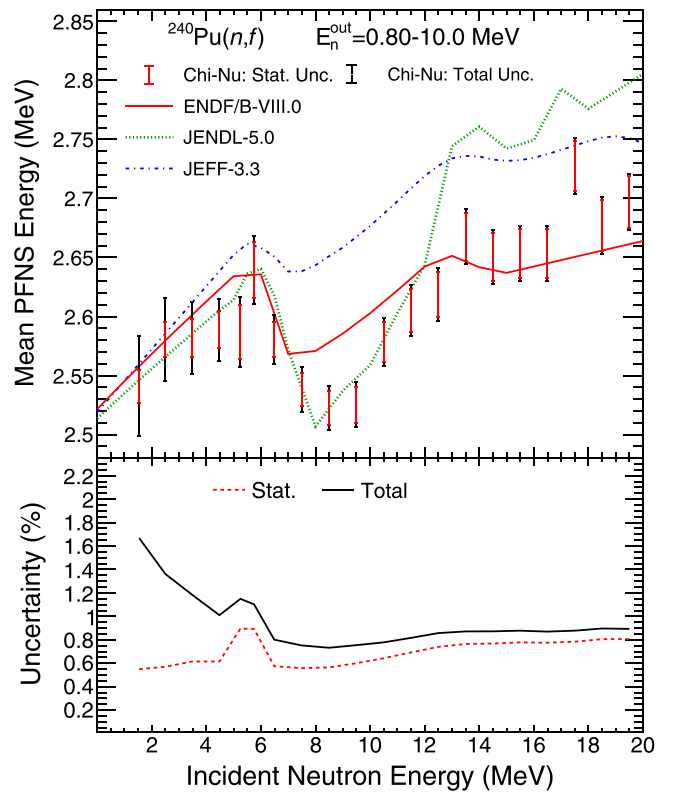

FIG. 10. Mean PFNS energies are a function of E_n^{inc} are shown in the top panel with the total (black) and statistical (red) uncertainties of the data reported here. ENDF/B-VIII.0, JEFF-3.3, and JENDL-5.0 mean energies are shown as the solid red, dash-dotted blue, and dotted green lines, respectively. The trends of total (solid black lines) and statistical (dashed red line) uncertainties of the present results are shown in the bottom panel.

ever, the JEFF-3.3 evaluation strongly deviates in $\langle E \rangle$ from the data in this range where second-chance fission becomes possible, while the ENDF/B-VIII.0 and JENDL-5.0 evaluations both appear to agree well with the data. This increase in $\langle E \rangle$ relative to the data and other evaluations was also observed and discussed in the neutron spectra themselves in Sec. IV C. In this range, the ENDF/B-VIII.0 library displays a minimum $\langle E \rangle$ at approximately $E_n^{\mathrm{inc}} = 7.0$ MeV, whereas the data and the JENDL-5.0 evaluation show minima closer to $E_n^{\mathrm{inc}} = 8.0$–9.0 MeV.

Approaching the threshold for third-chance fission, the $\langle E \rangle$ of the data increases from $E_n^{\mathrm{inc}} = 9.0$–13.0 MeV similar to the increase predicted by JENDL-5.0, though the ENDF/B-VIII.0 evaluation predicts less of an increase through this energy range. While the JEFF-3.3 and ENDF/B-VIII.0 libraries are offset from each other above $E_n^{\mathrm{inc}} = 8.0$ MeV by approximately 100 keV in $\langle E \rangle$, the shapes of these evaluations are nearly identical after separating near the second-chance fission threshold. This shape agreement could be related to the similar lack of pre-equilibrium neutron emission, but also likely related to the similar magnitude of the third-chance fission process in these evaluations.

The flattening of the measured $\langle E \rangle$ trends and the hint of a slight drop in $\langle E \rangle$ from $E_n^{\mathrm{inc}} = 13.0$–15.0 MeV is potentially

indicative of third-chance fission, and is an experimental observation of this feature in the data. Interestingly, the relatively minor drop in $\langle E \rangle$ for this feature is similar to ^{239}Pu(n, f) results from Ref. [15], and is less than the observed decrease in the ^{235}U(n, f) [16] and ^{238}U(n, f) [17] measurements, all of which were made with a nearly identical setup to that used for this work. Although JENDL-5.0 broadly appears to agree best with the present results until $E_n^{\text{inc}} \approx 12$ MeV, ENDF/B-VIII.0 agrees well with the present results at the highest incident energies.

V. CONCLUSIONS

The common presence of ^{240}Pu in nuclear fuels has resulted in enhanced interest in nuclear data on this nucleus. Measurements of neutron spectra from ^{240}Pu are notoriously difficult owing to the high α emission probability and the presence of spontaneous fission. These difficulties have resulted in an overall lack of experimental PFNS measurements, with only one neutron-induced PFNS measurement (at $E_n^{\text{inc}} = 0.85$ MeV) and two spontaneous fission PFNS measurements, only one of which reported uncertainties for the spectrum itself. Both the in-beam and spontaneous fission data were reported as a direct ratio to ^{252}Cf(sf) as well. This lack of data has made reliable nuclear data evaluations difficult, resulting in the ENDF/B-VIII.0 library, for example, relying primarily on measurements of neutron multiplicity from fission for PFNS evaluations.

This work reports a new ^{240}Pu(sf) PFNS measurement, and the first measurements of the ^{240}Pu(n, f) PFNS above $E_n^{\text{inc}} = 0.79$ MeV, spanning $E_n^{\text{inc}} = 1.0$–20.0 MeV, as part of the Chi-Nu PFNS experiment collaboration between Los Alamos National Laboratory and Lawrence Livermore National Laboratory. Clear evidence of second-chance fission and pre-equilibrium neutron emission processes were seen in the spectrum results. The average PFNS energies showed evidence of second-chance fission as well as a smaller con-

tribution from third-chance fission, the latter of which was difficult to observe in the spectra directly. JENDL-5.0 is the only nuclear data evaluation library containing both multichance fission and pre-equilibrium neutron emission processes (others such as ENDF/B-VIII.0 and JEFF-3.3 contain multichance fission, but not pre-equilibrium) and, in general, the present results broadly agree with the JENDL-5.0 evaluation. However, there are also clear differences observed in the spectra relating to the magnitude of second-chance fission in the data, as well as a possible energy shift in the thresholds relating to the pre-equilibrium neutron emission process preceding fission.

These data add to the collection of PFNS results obtained under the Chi-Nu experimental campaign which includes measurements on ^{235}U [16], ^{238}U [17], and ^{239}Pu [15] targets. All of these results also were measured in consistent experimental environments. However, the complications posed by the ^{240}Pu target nucleus mentioned above resulted in a slightly different experimental approach, focusing only on higher emitted neutron energies from fission ($E_n^{\text{out}} = 0.79$–10.0 MeV for this work, as opposed to $E_n^{\text{out}} = 0.01$–10.0 MeV for the other nuclei mentioned above).

[1] G. Palmiotti and M. Salvatores, J. Nucl. Sci. Technol. **48**, 612 (2011).

[2] G. Palmiotti, M. Salvatores, G. Aliberti, M. Herman, S. D. Hoblit *et al.*, Nucl. Data Sheets **118**, 596 (2014).

[3] F. Bostelmann, G. Ilas, and W. A. Weiselquist, Oak Ridge National Laboratory Report No. ORNL/TM-2020/1557 (US DOE, USA, 2020).

[4] F. Bostelmann, G. Ilas, and W. A. Weiselquist, J. Nucl. Eng. **2**, 345 (2021).

[5] G. Aliberti, G. Palmiotti, M. Salvatores, and C. G. Stenberg, Nucl. Sci. Eng. **146**, 13 (2004).

[6] D. A. Brown, M. B. Chadwick, R. Capote, A. C. Kahler, A. Trkov *et al.*, Nucl. Data Sheets **148**, 1 (2018).

[7] Z. A. Alexandrova, V. I. Bolshov, V. F. Kuznetsov, G. N. Smirenkin, and M. Z. Tarasko, Sov. Atmoic Energy **36**, 355 (1974).

[8] B. Gerasimenko, L. Drapchinsky, O. Kostochkin, T. Kuzmina, N. Skovorodkin, and V. Trenkin, J. Nucl. Sci. Technol. **39**, 362 (2002).

[9] A. B. Smith, P. T. Guenther, G. Winkler, and R. McKnight, Nucl. Sci. Eng. **76**, 357 (1980).

[10] R. Capote, Y.-J. Chen, F.-J. Hambsch, N. V. Kornilov, J. P. Lestone *et al.*, Nucl. Data Sheets **131**, 1 (2016).

[11] J. E. Simmons, R. B. Perkins, and R. L. Henkel, Phys. Rev. **137**, B809 (1965).

[12] F. Tovesson, T. S. Hill, M. Mocko, J. D. Baker, and C. A. McGrath, Phys. Rev. C **79**, 014613 (2009).

[13] A. S. Vorobyev, A. M. Gagarski, O. A. Shcherbakov, L. A. Vaishene, and A. L. Barabanov, JETP Lett. **112**, 323 (2020).

[14] K. J. Kelly, T. Kawano, J. M. O'Donnell, J. A. Gomez, M. Devlin *et al.*, Phys. Rev. Lett. **122**, 072503 (2019).

[15] K. J. Kelly, M. Devlin, J. M. O'Donnell, J. A. Gomez, D. Neudecker *et al.*, Phys. Rev. C **102**, 034615 (2020).

[16] K. J. Kelly, J. A. Gomez, M. Devlin, J. M. O'Donnell, D. Neudecker *et al.*, Phys. Rev. C **105**, 044615 (2022).

[17] K. J. Kelly, M. Devlin, J. M. O'Donnell, D. Neudecker, A. E. Lovell *et al.*, Phys. Rev. C **108**, 024603 (2023).

[18] P. W. Lisowski and K. F. Schoenberg, Nucl. Instrum. Methods Phys. Res. A **562**, 910 (2006).

[19] C. Y. Wu, R. A. Henderson, R. C. Haight, H. Y. Lee, T. N. Taddeucci *et al.*, Nucl. Instrum. Methods Phys. Res. A **794**, 76 (2015).

[20] https://www.caen.it/products/v1730 (2020).

[21] https://eljentechnology.com/products/liquid-scintillators/ej-301-ej-309.

[22] H. Y. Lee, T. N. Taddeucci, R. C. Haight, T. A. Bredeweg, A. Chyzh *et al.*, Nucl. Instrum. Methods Phys. Res. A **703**, 213 (2013).

[23] T. N. Taddeucci, R. C. Haight, H. Y. Lee, D. Neudecker, J. M. O'Donnell *et al.*, Nucl. Data Sheets **123**, 135 (2015).

[24] M. Devlin, J. A. Gomez, K. J. Kelly, R. C. Haight, J. M. O'Donnell *et al.*, Nucl. Data Sheets **148**, 322 (2018).

[25] J. M. O'Donnell, Nucl. Instrum. Methods Phys. Res. A **805**, 87 (2016).

[26] K. J. Kelly, J. M. O'Donnell, J. A. Gomez, M. Devlin, and E. A. Bennett, Nucl. Instrum. Methods Phys. Res. A **1045**, 167531 (2023).

[27] M. Devlin, K. J. Kelly, J. A. Gomez, J. M. O'Donnell, D. Neudecker *et al.*, EPJ Web of Conf. **284**, 04007 (2023).

[28] K. J. Kelly, J. M. O'Donnell, J. A. Gomez, T. N. Taddeucci, M. Devlin *et al.*, Nucl. Instrum. Methods Phys. Res. A **866**, 182 (2017).

[29] K. J. Kelly, M. Devlin, J. M. O'Donnell, D. Neudecker, and E. A. Bennett, Nucl. Instrum. Methods Phys. Res. A **1010**, 165552 (2021).

[30] K. J. Kelly, M. Devlin, J. A. Gomez, J. M. O'Donnell, T. N. Taddeucci *et al.*, EPJ Web Conf. **193**, 03003 (2018).

[31] P. Talou, I. Stetcu, P. Jaffke, M. E. Rising, A. E. Lovell, and T. Kawano, Comput. Phys. Commun. **269**, 108087 (2021).

[32] K. J. Kelly, J. M. O'Donnell, D. Neudecker, M. Devlin, and J. A. Gomez, Nucl. Instrum. Methods Phys. Res. A **943**, 162449 (2019).

[33] A. J. Plompen, O. Cabellos, C. De Saint Jean, M. Fleming, A. Algora *et al.*, Eur. Phys. J. A **56**, 181 (2020).

[34] K. Shibata, O. Iwamoto, T. Nakagawa, N. Iwamoto, A. Ichihara *et al.*, J. Nucl. Sci. Technol. **48**, 1 (2011).

[35] M. B. Chadwick, M. Herman, P. Oblozinský, M. E. Dunn, Y. Danon *et al.*, Nucl. Data Sheets **112**, 2887 (2011).

[36] OECD NEA Data Bank, JEFF-3.2 Evaluated Data Library–Neutron Data, http://www.oecd-nea.org/dbforms/data/eva/evatapes/jeff_32/ (2014).